



Contents lists available at ScienceDirect

Scripta Materialia

journal homepage: [www.elsevier.com/locate/scriptamat](http://www.elsevier.com/locate/scriptamat)

Viewpoint set

## Viewpoint: Nanoscale chemistry and crystallography are both the obstacle and pathway to advanced radiation-tolerant materials☆

Chad M. Parish\*, Kun Wang, Philip D. Edmondson

Nuclear Materials Science and Technology Group, Materials Science and Technology Division, Oak Ridge National Laboratory, Oak Ridge, TN, USA

### ARTICLE INFO

#### Article history:

Received 22 January 2017

Received in revised form 10 May 2017

Accepted 10 May 2017

Available online xxxx

#### Keywords:

Radiation damage

Atom probe

Scanning transmission electron microscopy

Multivariate statistical analysis

Transmission Kikuchi diffraction

### ABSTRACT

New candidate materials for GenIV or fusion nuclear energy systems, e.g., nanostructured ferritic alloys, are distinguished from older-generation nuclear materials by much smaller feature sizes and complex local nanochemistry and crystallography. Established and perspective nuclear materials, e.g. reactor pressure vessel steels or plasma-facing tungsten, also form small nanoscale structures under in-reactor service. Here, we discuss recent advances in materials characterization – high-efficiency X-ray mapping combined with datamining; transmission Kikuchi diffraction; and atom probe tomography – that make it possible to quantitatively characterize these nanoscale structures in unprecedented detail, which enables advances in understanding and modelling of radiation service and degradation.

© 2017 Acta Materialia Inc. Published by Elsevier Ltd. All rights reserved.

### 1. Introduction

Materials long have been, and remain, the main obstacle to advanced reactor concepts [1]. Only with new more-radiation-tolerant materials can nuclear energy move on from the 1960s technology dominating the present fleet into true a 21st-century technology. Three broad methods have been proposed to improve the radiation tolerance of materials [2]: (1) choose or design a material with an intrinsically radiation-tolerant matrix phase. (2) Choose or design a material in which vacancies or interstitials are immobile at the service temperature. (3) Choose or design a material with engineered high sink strength, which is to say, a nanoengineered material. Broadly speaking, strategy (3) is under the most research in the modern nuclear materials community, and even approaches emphasizing strategies (1) or (2) will often incorporate nanostructuring.

Nanoengineering and nanostructuring, then, are the main pathway forward to advanced nuclear materials that can withstand the conditions envisioned for future reactors. However, nanostructuring poses distinct obstacles to experimental characterization, making it difficult

to identify in sufficient quantitative detail microstructural processes that are occurring under irradiation. What new tricks and tools, available to the microscopist, will help us move the radiation-tolerant materials community forward? We attempt to provide our viewpoint to that question in this article.

As an example, compare and contrast 316 stainless steel (SS), the archetypical example of Generation-II (GenII) in-core reactor structural materials, to nanostructured ferritic alloy (NFA) 14YWT [3,4], the archetypical example candidate material for GenIV or fusion systems. First, the ferritic (BCC) 14YWT matrix is more inherently radiation-resistant in contrast to the austenitic (FCC) 316SS matrix [2]. Second, the contrast *in size scale*: 316SS has grain sizes of tens to hundreds of microns, and large precipitates (100 s of nm or more). In 14YWT, grain sizes are a small fraction of a micron, with nano-scale precipitates (certainly  $\ll 10$  nanometers) that serve to pin the grain boundaries and act as strong sinks for migrating point defects and He produced by transmutation [5]. Which is to say, the materials of interest for future reactors have nanostructure sizes at least three orders of magnitude smaller than those of current-generation reactors.

As feature sizes shrink, characterization of the features becomes progressively more difficult. Nuclear materials, in particular, undergo multiple simultaneous modes of microstructural evolution under irradiation, and quantifying the microstructure under radiation damage is an absolute necessity to model and predict the changes in physical properties, such as fracture toughness, vital for regulatory approval and safe operation of future-generation reactors.

So, our thesis for this Viewpoint: *although the traditional methods of electron microscopy developed in the early days of radiation materials science [6,7] are well-suited to the materials studied in the early days of*

☆ Notice: This manuscript has been authored by UT-Battelle, LLC under Contract No. DE-AC05-00OR22725 with the U.S. Department of Energy. The United States Government retains and the publisher, by accepting the article for publication, acknowledges that the United States Government retains a non-exclusive, paid-up, irrevocable, world-wide license to publish or reproduce the published form of this manuscript, or allow others to do so, for United States Government purposes. The Department of Energy will provide public access to these results of federally sponsored research in accordance with the DOE Public Access Plan (<http://energy.gov/downloads/doe-public-access-plan>).

\* Corresponding author.

E-mail address: [parishcm@ornl.gov](mailto:parishcm@ornl.gov) (C.M. Parish).

radiation materials science, modern nanostructured materials must be analyzed with modern nanocharacterization methods. Perhaps this is tautological, and we've made some of these arguments already [8–10], but here we expand upon these thoughts. Specifically, we (1) describe how applications of the new analytical hardware and software available to materials scientists makes unprecedented levels of detail available at nanometer-level size scales, and (2) try to speculate upon how these techniques might lead to breakthroughs in radiation materials science in the near future.

Electron microscopy is thriving currently, thanks to ever-improving computers and related improvements such as analytical detectors and electron-optical aberration correctors. We will emphasize only three methods in order to keep this Viewpoint short, but these are the three methods we think are most likely to drive near-term advances in radiation materials science understanding and attendant materials design. These three methods are: scanning transmission electron microscopy X-ray mapping (STEM-EDS); transmission Kikuchi diffraction (tKD); and atom probe tomography (APT).

These three methods, in their latest incarnations, are illustrated in Fig. 1. The various vendors' latest generation analytical electron microscopes [11–13] (in the case of Fig. 1a–c, the FEI Talos F200X STEM) incorporate bright electron optics and multiple large X-ray detectors, which provide improvements of around 100× in terms of X-ray collection compared to instruments available a few years ago. Fig. 1c illustrates the importance of advanced data analysis: correlations unexpected by the analyst, or too small to see using standard analysis techniques, are discovered by computational datamining. Both advanced X-ray mapping (Fig. 1a) and computational data analysis (Fig. 1c) will be discussed below. The next of the three techniques we wish to discuss, tKD [14–16], is illustrated in Fig. 1d. Here, the highly nanocrystalline grain size of 14YWT is seen in the crystallographic map. Combining STEM-EDS and all its modern capabilities with tKD allows a tremendously comprehensive and quantitative analysis of the specimens. In terms of radiation materials science, local chemistry, grain boundary character, and precipitate character all link to the ability of a

material to retain its properties and survive radiation service. APT complements both tKD and STEM-EDS by combining a higher quantification precision, and finer spatial resolution, and some crystallographic capabilities [17].

Briefly, let's illustrate our thesis using Fig. 1. A focused-ion-beam (FIB) prepared thin foil of 14YWT NFA (ORNL heat SM10) was analyzed in the Talos F200X STEM [18] by X-ray spectrum imaging. This sample was Pt-ion irradiated to ~160 dpa at –100 °C [19,20], and the EDS map is from below the irradiated region. From the spectrum image, the X-ray counts for W-L $\alpha$ , Ti-K $\alpha$ , and Y-L $\alpha$  were extracted, false colored, and presented as Fig. 1a. This shows a complex array of microstructural features: W grain boundary segregation (as well as Cr, not shown for easier readability), and Y-Ti-rich and Ti-rich precipitates, in different sizes. The accompanying HAADF-STEM image is Fig. 1b. A multivariate statistical analysis (MVSA) decomposition of the EDS SI, using the Sandia National Laboratories AXSIA code [21], separates Cr-W segregation, Ti precipitate component, and Y-O precipitate components very clearly. This statistical decomposition denoises the data, finds the correlations (such as Cr-W at the grain boundaries and Ti-Y-O in the precipitates), providing a tremendously improved qualitative analysis of the elemental signals. MVSA also finds components the human analyst might not have looked for: aluminum is not deliberately added to the alloy, but Al-Ti-O precipitates appear in the MVSA map. In Fig. 1d, tKD is taken using the same TEM foil and a standard EBSD system. The foil is held in a special holder and raised until it nearly touches the SEM objective lens, and then maps are acquired using the EBSD hardware and software, but capturing the transmitted patterns that have passed through the foil. This provides an EBSD-like crystallographic map, but with tremendously improved spatial resolution. In Fig. 1c, pixels are 5 nm, and features down to <40 nm are easily seen. APT is a technique capable of providing highly spatially and chemically resolved three-dimensional atom-by-atom rendering of a materials specimen, with a unique ability to resolve the chemical identities of atoms, even at extremely dilute concentrations or very light species that are not easily distinguishable via electron microscopy based techniques. A

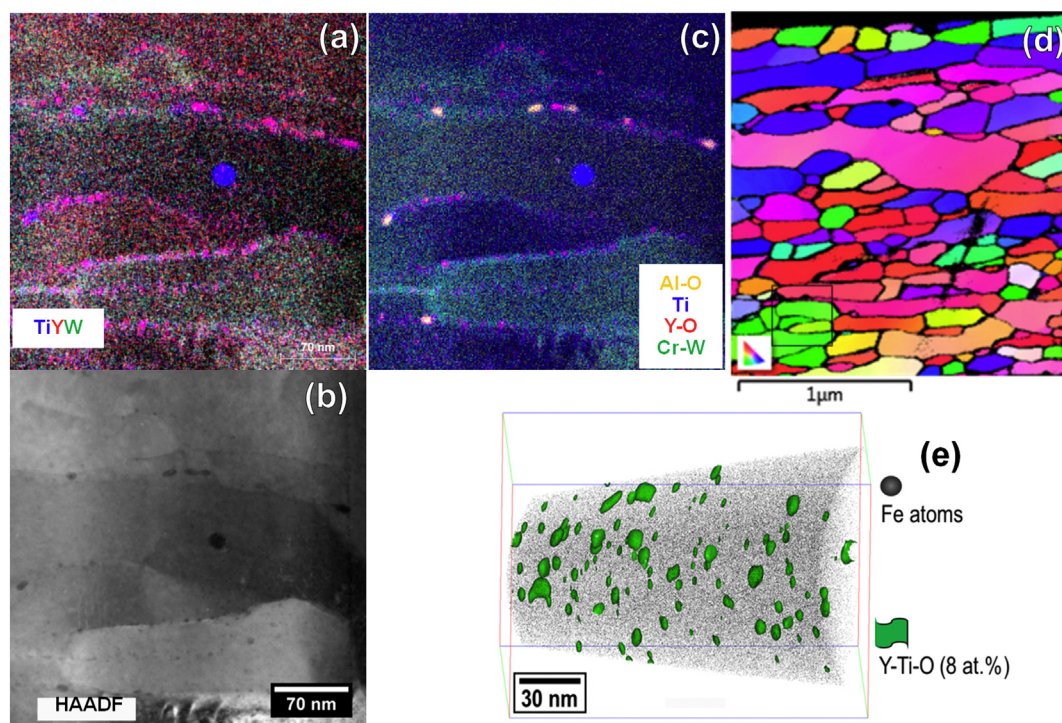


**Fig. 1.** (a) Colored X-ray maps (Ti, Y, W) of 14YWT alloy. (b) HAADF image of the same region. (c) Colored score images from multivariate statistical analysis of the same dataset as (a); an unexpected Al-O rich phase is discovered via this datamining. (d) tKD map, colored on the out-of-page direction; the black box denotes the region of (a)–(c). (e) APT image of 14YWT alloy (see online Supplementary information Fig. S1 for details). (a) has a 3 × 3 pixel smoothing filter applied. (c) is binned 4 × 4 pixels, from 1024<sup>2</sup> to 256<sup>2</sup> pixels. (For interpretation of the references to color in this figure legend, the reader is referred to the web version of this article.)



representative atom map data taken from a 14YWT specimen (ORNL heat SM6) showing the Fe atoms in the matrix (black dots) and the nano-scale oxide dispersoids (concentration isosurfaces shown in green) is shown in Fig. 1e. The nano-scale dispersoids are easily identifiable, and the data can then be explored using a multitude of analysis methods to obtain information on features such as the dispersoid composition, size and morphology; and other features such as segregation of solutes to dislocations etc. (not described here) [17].

## 2. Advanced electron microscopy

Nanostructuring either can be by design, as in the 14YWT alloy above, or can occur incidentally during irradiation. Tungsten is the leading candidate for fusion tokamak divertors and other plasma-facing components, but undergoes tremendous transmutation under neutron irradiation; this transmutation, in turn, results in evolution of solute-rich nanoprecipitates in the tungsten matrix. Previous work, using TEM methods, has begun to explore this irradiation-induced structure [22–24]. Very small (~10 nm) precipitates appear in tungsten irradiated to ~3 dpa, ~700 °C in a mixed-spectrum reactor (Oak Ridge High Flux Isotope Reactor, HFIR). A HAADF image (Fig. 2a), raw X-ray maps (Fig. 2b–d), and MVSA datamined results (Fig. 2e–h) indicate an extremely complex structure evolved during irradiation.

Specifically, the matrix is tungsten, but contains a number of irradiation-induced voids (black circles in HAADF). Precipitates form copiously in the matrix, as seen by the Re and Os maps. The maps in Fig. 2b–d are  $800^2$  pixels, or  $6.4 \times 10^5$  pixels. This is a tremendous quantity of data ( $\approx 1.3$  billion individual data elements at 2048 channels/pixel); with the recently retired instrument in our lab, a Philips CM200FEG, a typical X-ray map might consist of  $50 \times 50$  to  $100 \times 100$  pixels, a factor of 64–256× smaller! (see Table 1). The aggregate X-ray count rates typical on that instrument, with a single small Si(Li)-type X-ray detector, were 1–5 kcps (kilocounts per second), compared to 90 kcps in the

**Table 1**

Comparisons of different STEM X-ray mapping capabilities; these are common values. Data size calculated assuming 2048 spectral channels/pixel, and 4 bytes/channel.

Instrument	CM200	F200X
Map time	1 h	
Area mapped	500 nm × 500 nm	
Pixels	50 × 50	1024 × 1024
s/pixel	1.4	0.003
nm/pixel	10	0.5
Counts/s	1000	100,000
Counts, total	3,600,000	360,000,000
Counts/pixel	1440	343
Counts/nm <sup>2</sup>	14.4	1440
Data produced, MB	19.5	8192

data of Fig. 2, taken on the F200X instrument now in our laboratory. A typical CM200 map might have used about the same pixel size (~1 nm), in order to still interrogate the small (<10 nm) features, and would therefore have covered a far smaller fraction of the region of interest. The data in Fig. 2 shows the microstructure's different features, such as radiation-induced segregation (RIS), radiation induced precipitation (RIP), and precipitate denuded zones (DZs), clearly and at a glance. The magnitudes of difference are illustrated, using typical experimental values, in Table 1. On the CM200, a dozen or more individual maps would have been needed, with the possibility of unconscious selection bias missing certain features or regions.

Perhaps an underappreciated difference between older and newer instruments is in the quantity of data produced, rather than the easier-to-see qualitative improvement in the data. The last row of Table 1 illustrates that the amount of data produced increases by a factor of over 400×! The corollary to this, which we argue is underappreciated in our field, is that a human cannot reasonably expect to interrogate such a massive dataset manually. This is where the recent advances in MVSA methods become indispensable.

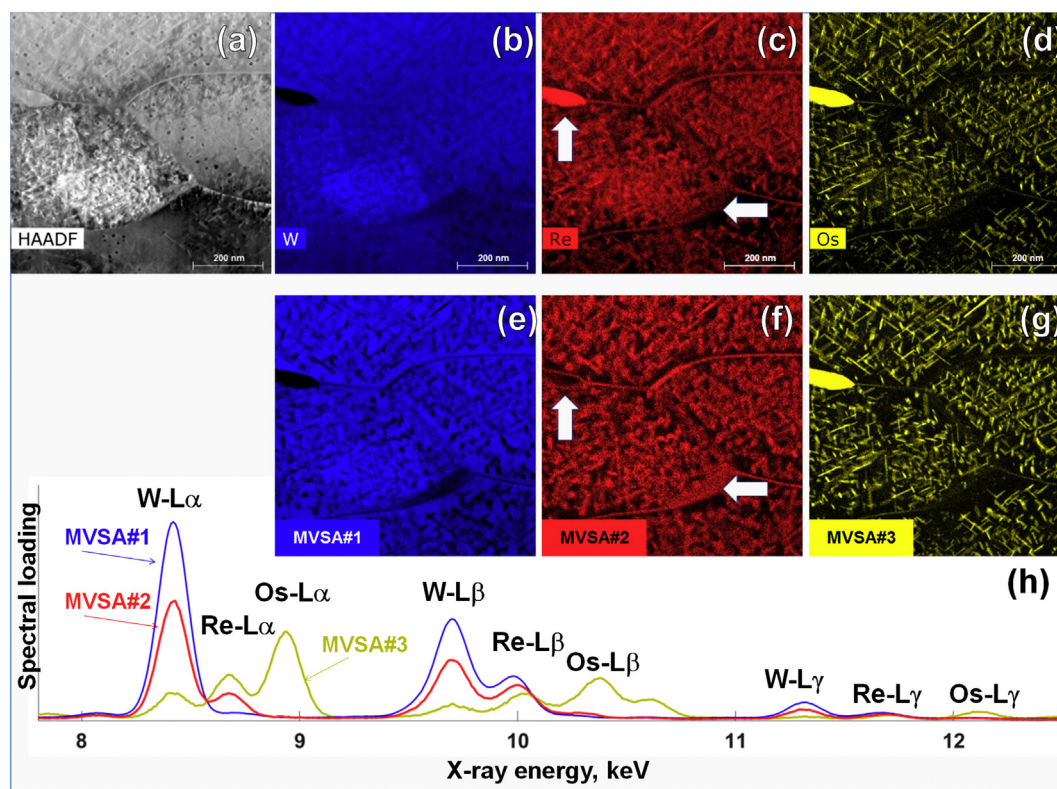


**Fig. 2.** (a) HAADF and (b–d)  $L\alpha$ -line X-ray maps from a STEM spectrum image.  $3 \times 3$  pixel averaging filter applied. (e–g) Score images and (h) loading spectra from MVSA analysis of the same dataset. (e–g) are binned  $2 \times 2$  pixels. (For interpretation of the references to color in this figure, the reader is referred to the web version of this article.)

At first glance, Fig. 2b–d (the X-ray maps) and Fig. 2e–g (the MVSA score images) look the same; but the MVSA images actually provide far more insight, once we examine them. The matrix (blue) MVSA score image, Fig. 2e, provides much higher contrast and lower noise than the W map (Fig. 2b), as a result of the signal aggregation inherent to MVSA methods. The second (red) MVSA component, as seen in the loading spectrum (Fig. 2h) is strong in W X-ray counts with a smaller amount of Re counts, indicating that – because the small precipitates are thinner than the TEM foil, and presumably a W-Re-Os intermetallic – any pixel containing the secondary phases will contain both W and Re atoms. The large grain-boundary precipitate ( $\uparrow$  arrow in Fig. 2c and f) appears different in the MVSA#2 score image vs. the Re X-ray map: in the Re X-ray map, the precipitate is solid, but the MVSA#2 component shows a ring around the precipitate perimeter. Comparing with the MVSA#3 component (yellow, Fig. 2g) and the Os map (Fig. 2d), they appear quite similar, and the MVSA#3 loading spectrum (Fig. 2h) indicates the MVSA#3 component is strong in Os, but also contains significant X-ray counts from Re and W. This means that the large precipitate has an Os-rich, Re- and W-bearing center, but a Re-rich ring around its edge. This insight might be found using conventional methods by extracting a line profile across the precipitate, but the MVSA actually tells us to look for this

core/shell structure! An overlay of the MVSA#2 and MVSA#3 components, Fig. 3a, shows that the Os-rich MVSA#3 is located in the center of the needle-like precipitates, and the Re-W enriched MVSA#2 across each precipitate, showing another core-shell type structure. Because these core/shell structures are only slight variations in the solute atoms' ratios, and not a gross segregation, simply overlaying the X-ray count signals (Fig. 3b) does not provide this same level insight.

Summarizing, modern STEM systems are capable of simply unprecedented X-ray mapping capability, in terms of both the number of raw signal counts collected, and in terms of the density and size of the data obtained. MVSA methods – of which there are many, and we emphasize only a small family here [25] – provide noise filtering, signal aggregation, qualitative analysis, and will often find small signals or local variations the analyst would not look for without the computer's unbiased statistical analysis discovering small and non-obvious variances within the huge dataset.

### 3. Transmission Kikuchi diffraction

Transmission Kikuchi diffraction, tKD, is a derivative of the well-known electron backscatter diffraction (EBSD) technique. The difference is that in tKD, a thin-foil TEM sample is used, and the diffraction patterns captured are collected from the electron-beam exit surface of the foil (hence “transmission”), whereas in EBSD the diffraction patterns are collected from the electron-beam entrance surface (hence “backscatter”) of a thick sample. tKD is a very new method [14], and its capabilities and limitations are still very much under exploration [15,16,26–28]. We have only begun applying it to our problems recently, but it appears that this will be a tremendous adjunct to S/TEM methods, as well as a powerful stand-alone tool (e.g.[29,30]).

Continuing our theme for this Viewpoint, tKD is most powerful when used as a direct complement to S/TEM methods. Advanced S/TEM, above, collects prodigious quantities of spatially resolved elemental data. Performing tKD on the same region of a thin foil will quickly collect the matching crystallographic information. Combining these two nanometer-scale techniques – elemental and crystallographic – produces information not readily available to either method alone.

tKD of the same region as Figs. 2–3 is seen in Fig. 4; the grains observed by STEM in Figs. 2–3 are marked with a square box (for experimental details, including the “cleanup” [31] procedure, see online Supplementary information). Many different microstructural details can be obtained from tKD and EBSD datasets. In the interest of space, we will emphasize grain boundary character here. The white boundary

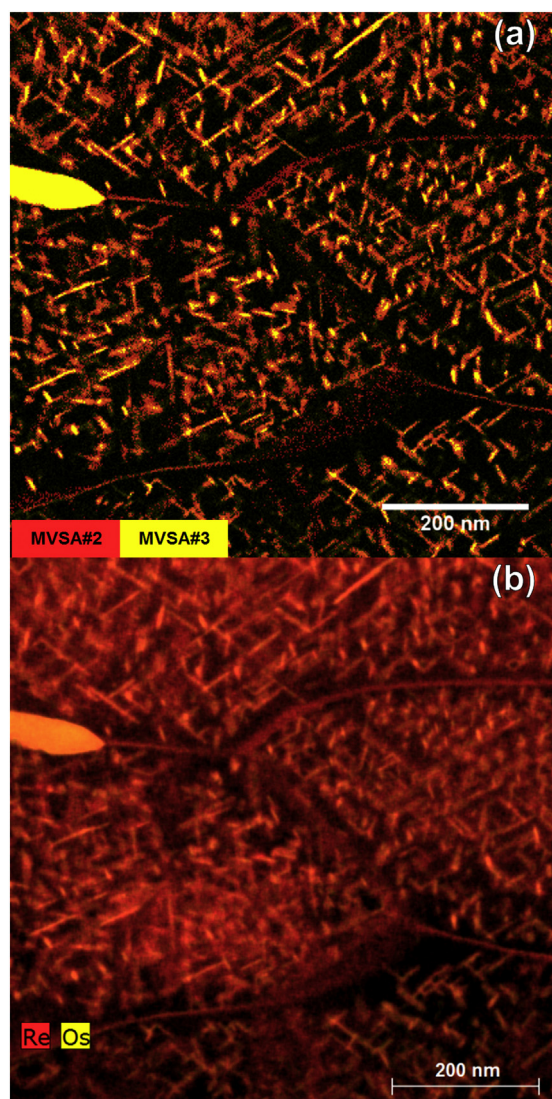


**Fig. 3.** (a) Color overlay of MVSA component #2 (W-Re, red) and #3 (Os-Re, yellow). Binned  $2 \times 2$  pixels. (b) Color overlay of Re-L $\alpha$  and Os-L $\alpha$  X-ray counts,  $3 \times 3$  pixel smoothing filter. (For interpretation of the references to color in this figure legend, the reader is referred to the web version of this article.)

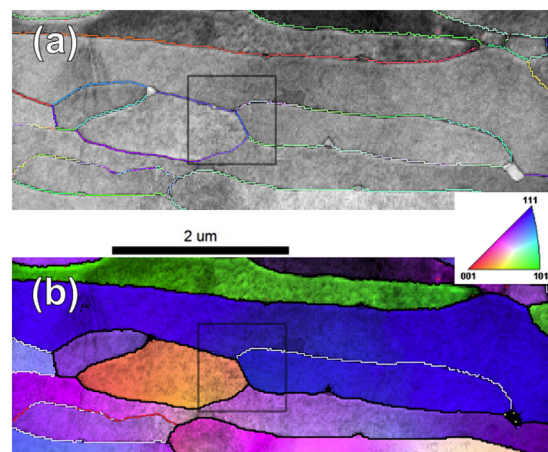


**Fig. 4.** tKD maps of the neutron-irradiated tungsten sample. (a) Image quality map. Grain boundaries are colored according to the misorientation axis, as seen on the unity triangle. (b) Out-of-the-page inverse pole figure colored map, using the same unit triangle coloring. Grain boundaries are colored as 2–5° (red), 5–15° (white), and >15° (black). Shaded gray squares are the region of Figs. 2–3. (For interpretation of the references to color in this figure legend, the reader is referred to the web version of this article.)



in the STEM analyzed region shows approximately a  $7^\circ$  misorientation around the  $\langle 325 \rangle$  axis, and the black boundaries  $40\text{--}60^\circ$  misorientations around several different axes. What is relevant about grain boundary misorientations? In most irradiated materials, RIS varies non-monotonically with the grain boundary misorientation and will usually decrease at special grain boundaries, such as twins [32]. In Figs. 2–3, we see that the RIS of Re-Os is not markedly different at the medium-angle ( $7^\circ$ ) or high-angle ( $40\text{--}60^\circ$ ) boundaries, indicating that in this system, thermomechanical processing to emphasize low-angle boundaries would not reduce RIS. Whether RIS has a detrimental effect on mechanical or thermal properties in this system is still unknown, but this is a question that will need to be addressed in future studies. Another question to ask is if special or coincident-site-lattice (CSL) boundaries would reduce RIS; searching for boundaries of particular character via tKD would be trivial and would allow interrogation of hundreds of boundaries in an hour or two (much less time than is required to produce a FIB foil from the highly radioactive bulk starting specimen!). Advanced STEM methods, as above, could then interrogate these special boundaries, and a matching set of random boundaries for comparison, in a few hours, as well. Another interesting question is if grain boundary character can encourage or discourage either RIP or DZ formation. These topics will be explored in future experiments.

An important comparison to tKD is the method of precession electron diffraction, which provides similar data but is performed in TEM, using a high-speed camera to capture precession electron diffraction patterns in a scanned raster array [33–36]. PED is especially valuable because it can be performed in TEM, potentially not requiring transfer to an SEM after S/TEM analytical mapping, and can provide slightly improved spatial resolution compared to tKD. We have used PED in conjunction with tKD and find it a powerful adjunct [30]. However, the simplicity of tKD, the ready availability of EBSD systems in many laboratories, and easier indexing allowed by the larger slice of reciprocal space captured by an EBSD camera in tKD compared to a TEM camera in PED, means that tKD is often easier and faster than PED, although ideally a laboratory would have both systems at hand.

Summarizing, tKD is a new enough technique that we really don't know its full capabilities or most exciting applications. However, in the next few years, in conjunction with advanced STEM methods, tKD will revolutionize the study of grain boundary effects on radiation-driven microstructural processes, such as RIS, RIP, and radiation creep.

#### 4. Atom probe tomography

The local electrode atom probe (LEAP) is a technique capable of providing highly spatially and chemically resolved three-dimensional data about a materials system, with the unique ability to resolve the chemical species of the atoms that constitute the material. A typical atom map from a 14YWT nanostructured ferritic alloy was previously shown in Fig. 1e in which the matrix is represented by the Fe atoms shown in black, and the oxide dispersoids are highlighted through the use of

concentration isosurfaces (8 at.% Y-Ti-O). In this example the material has been joined using technique of friction stir welding, followed by ion irradiation (ion irradiation conditions were 2.75 MeV Fe<sup>+</sup>, 250 °C,  $5.2 \times 10^{20}$  ions m<sup>-2</sup>) with the characterization being performed on the stir zone.

The graphs presented in Fig. 5a and b represent a proximity histogram of the Y, Ti, and O composition of an average cluster (Fig. 5a); and the radius distribution histogram of the clusters in a typical dataset. The number density and volume fraction of the clusters is also given in Fig. 5c. From the proximity histogram, it can be seen that the clusters are typically enriched in oxygen ( $\approx 10$  at.%) and also have concentrations of Y and Ti to about 7.5 at.%. This allows for a comparison of previous data to evaluate the effect of combined friction stir welding and irradiation on nano-cluster stability. A previous atom probe study of the as-extruded 14YWT material yielded a cluster composition of Y  $\sim 7.5$ , Ti  $\sim 42.2$ , and O  $\sim 43.5$  at.% [37]; following friction stir welding of the same material the cluster composition was determined to be Y  $\sim 8.1$ , Ti  $\sim 11.2$ , and O  $\sim 22.0$  at.% [38]. This suggests that the Y is quite stable under these conditions, and the biggest instabilities occur with the Ti and O concentrations.

The data available from atom probe tomography is highly complementary to the other techniques described here: scanning transmission electron microscopy and transmission Kikuchi diffraction. Indeed, using the techniques in a combined manner, e.g. performing all three techniques on the same sample volume, offers the possibility of performing characterization on a sample that would have an unparalleled correlative data resulting in enhanced understanding of materials' response development. Many examples of this combination are available (e.g. [39]) and STEM and APT can productively be combined with tKD (e.g. [40,41]) or PED (e.g. [42]).

#### 5. Other considerations

Let's take a moment to digress, briefly, into other important considerations for future advances in characterization of nuclear materials. The major concern for any sort of advanced microscopy – STEM, tKD, APT, etc. – is always sample preparation. The focused ion beam (FIB) has become the STEM preparation tool of choice [43], and low-energy post-FIB Ar<sup>+</sup> ion milling is establishing itself as a helpful, sometimes necessary, adjunct to FIB [44,45]. For radioactive materials, FIB is especially helpful because of the massive reduction ( $\sim 10^8 \times$  or so) in the mass of a sample. For instance, the grip end of a sub-size tensile specimen might be  $\sim 10$  mm<sup>3</sup>, whereas a FIB foil is perhaps  $10\text{--}100$   $\mu\text{m}^3$  or less [46]. The small samples in our tungsten irradiation campaign are often  $10\text{--}100$  mrem/h at 30 cm even at low doses, due to tungsten's activation properties in HFIR's mixed-spectrum neutrons, which is a dangerous dose rate that requires specialized laboratories for hands-on work and lead vaults for sample interim storage. We used a FIB tool in a lead-lined room [47] to protect the operator from the specimen's field (sometimes  $\sim 1$  mrem/h outside the FIB chamber), so the only

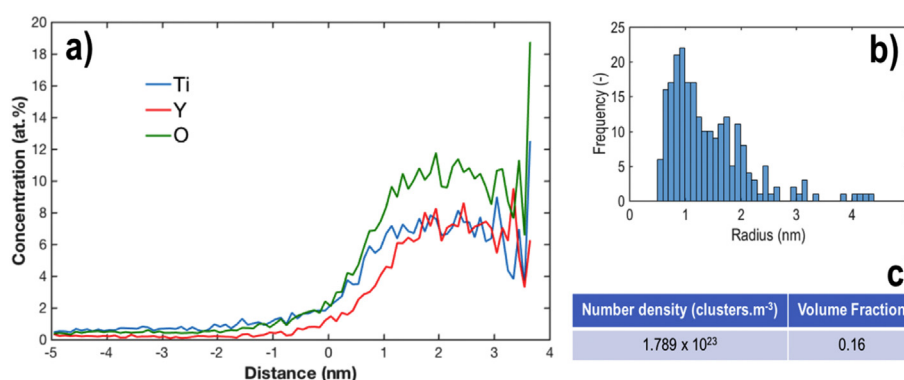


Fig. 5. Analysis of atom probe data in Fig. 1e. (a) Proximity histogram of the average compositions of the particles. (b) Histogram of particle radii. (c) Particle statistics.

dose acquired by the operator is during the few seconds the sample is exposed while being moved from its steel transportation “pig” to the FIB chamber. Once the FIB sample is thinned, we polished it in a Fischione Nanomill, which is a tool for removing the Ga-implantation and associated radiation damage from the higher-energy FIB beams [44].

Thus, specialized laboratories and attention to the hazards that make nuclear materials science distinct from other branches of materials science is also necessary for successful characterization of next-generation nuclear materials.

## 6. Perspective

Let's return to the thesis we stated earlier: *although the traditional methods of electron microscopy developed in the early days of radiation materials science are well-suited to the materials studied in the early days of radiation materials science, modern nanostructured materials must be analyzed with modern nanocharacterization methods.* Here, we described STEM-based X-ray mapping and its important companion, MVSA datamining; tKD nano-crystallographic mapping; and APT methods. Nanostructuring is becoming the dominant paradigm in producing materials that are more radiation resistant, and characterizing the way nanostructured materials respond to radiation damage requires interrogating much smaller features than in prior generations of radiation-tolerant nuclear materials. Luckily for us, new advances in electron microscopy and atom probe instrumentation and analytical methods are providing us with the tools we need.

Coordinated use of STEM X-ray mapping and tKD, we predict, will drive future advances in grain boundary engineering, radiation induced segregation, and related phenomena. STEM in conjunction with MVSA-based data mining will allow far more detailed and comprehensive interrogation of the many simultaneous phenomena (such as RIP, RIS, and radiation-induced phase instability), even across wide size scales. A modern STEM can easily acquire, for instance, a 5  $\mu\text{m}$ -wide X-ray map with 2.5 or 5 nm pixels, interrogating feature sizes across three orders of magnitude. MVSA datamining makes analysis of this copious data tractable.

The continued development of atom probe tomography instrumentation and analysis methods is driving the three-dimensional characterization of materials, allowing researchers to understand radiation effects with unprecedented clarity of spatial and chemical resolution. This enables a deeper understanding of the fundamentals of radiation damage and effects in existing materials such as precipitation/RIS/RIP; and to aid in the rapid development of more radiation tolerant materials such as those presented here.

Now for some predictions. Accident tolerant light-water fuel cladding and fuels are the major research thrust in the community at the moment [48]. We anticipate both FeCrAl-based and SiC-based cladding to be amenable to the methods discussed here, particularly for evolution of the oxide-based sintering additives in NITE-SiC [49], the matrix/fiber interface in SiC/SiC composites, and grain boundary character and chemistry under irradiation damage and irradiation creep in FeCrAl. ODS type steels, either FeCr (for fast reactors) or FeCrAl (for LWRs or fusion blankets) will also require high-resolution crystallography and chemical analysis by performing post-neutron-irradiation characterization to optimize their microstructures. Other problems we are addressing in our laboratory include NiMnSi-based precipitates in reactor pressure vessel steels [50,51], important for LWR life extension, and examination of high-burnup uranium-based fuels [52], and we are applying the methods discussed in this Viewpoint with exciting results we will publish soon.

In short, it's an exciting time to be studying nuclear materials, and the one thing we are sure of, is that the community will discover phenomena it didn't anticipate, and use these new experimental methods in ways that will surprise us all.

## Acknowledgements

CMP and KW supported by an Early Career Award, US Department of Energy, Office of Science, Fusion Energy Sciences. PDE supported by Department of Energy, Office of Nuclear Energy, Fuel Cycle R&D Program, and the Light Water Reactor Sustainability Program. We thank Dr. D. T. Hoelzer, ORNL, for the 14YWT specimens and Dr. Z. Feng, ORNL, for the welding. Work on 14YWT was supported by US Department of Energy, Office of Science, Basic Energy Sciences, Materials Science and Technology Division. Tungsten specimens part of the ORNL-University of Tennessee Office of Fusion Energy Sciences collaboration. FEI Talos F200X S/TEM provided by the Department of Energy, Office of Nuclear Energy, Fuel Cycle R&D Program and the Nuclear Science User Facilities. Part of this work (Fig. 1d, Fig. 5) supported by the U.S. Department of Energy, Office of Nuclear Energy under DOE Idaho Operations Office Contract DE-AC07-051D14517 as part of a Nuclear Science User Facilities Experiment.

## Appendix A. Supplementary data

Supplementary data to this article can be found online at <http://dx.doi.org/10.1016/j.scriptamat.2017.05.014>.

## References

- [1] D. Butler, *Nature* 429 (6989) (2004) 238–240.
- [2] S.J. Zinkle, L.L. Snead, *Annu. Rev. Mater. Res.* 44 (1) (2014) 241–267.
- [3] M.K. Miller, C.M. Parish, *Mater. Sci. Technol.* 27 (4) (2011) 729–734.
- [4] D.A. McClintock, D.T. Hoelzer, M.A. Sokolov, R.K. Nanstad, *J. Nucl. Mater.* 386 (2009) 307–311.
- [5] P.D. Edmondson, C.M. Parish, Y. Zhang, A. Hallén, M.K. Miller, *Scr. Mater.* 65 (8) (2011) 731–734.
- [6] M.L. Jenkins, *J. Nucl. Mater.* 216 (1994) 124–156.
- [7] E. Kenik, *J. Nucl. Mater.* 216 (1994) 157–169.
- [8] C.M. Parish, M.K. Miller, *J. Nucl. Mater.* 462 (0) (2015) 433–442.
- [9] C.M. Parish, *Microsc. Microanal.* 21 (03) (2015) 706–724.
- [10] C.M. Parish, K.G. Field, A. Certain, J.P. Wharry, *J. Mater. Res.* 30 (9) (2015) 1275–1289.
- [11] P.G. Kotula, D.O. Klenov, H.S. von Harrach, *Microsc. Microanal.* 18 (4) (2012) 691–698.
- [12] D. Klenov, B. Freitag, H.S. von Harrach, A.J. D'Alfonso, L.J. Allen, *Microsc. Microanal.* 17 (Suppl. 2) (2011) 598–599.
- [13] P. Schlossmacher, D.O. Klenov, B. Freitag, H.S. von Harrach, *Microscopy Today* 2010 (July 2010) 14–20.
- [14] R.R. Keller, R.H. Geiss, *J. Microsc.* 245 (3) (2012) 245–251.
- [15] S. Suzuki, *JOM* 65 (9) (2013) 1254–1263.
- [16] P.W. Trimby, *Ultramicroscopy* 120 (0) (2012) 16–24.
- [17] M.K. Miller, R.G. Forbes, *Atom-probe tomography: the local electrode atom probe*, Springer, New York, 2014.
- [18] C.M. Parish, MT3FT-15OR0204122: Report on the Acquisition and Installation of FEI Talos F200X S/TEM, <http://www.osti.gov/servlets/purl/1234344/> 2015.
- [19] C.M. Parish, R.M. White, J.M. LeBeau, M.K. Miller, *J. Nucl. Mater.* 445 (1–3) (2014) 251–260.
- [20] C.M. Parish, P.D. Edmondson, Y. Zhang, M.K. Miller, *J. Nucl. Mater.* 418 (2011) 106–109.
- [21] P.G. Kotula, M.R. Keenan, J.R. Michael, *Microsc. Microanal.* 9 (1) (2003) 1–17.
- [22] A. Hasegawa, M. Fukuda, S. Nogami, K. Yabuuchi, *Fusion Eng. Des.* 89 (7–8) (2014) 1568–1572.
- [23] A. Hasegawa, M. Fukuda, K. Yabuuchi, S. Nogami, *J. Nucl. Mater.* 471 (2016) 175–183.
- [24] X. Hu, T. Koyanagi, M. Fukuda, N.K. Kumar, L.L. Snead, B.D. Wirth, Y. Katoh, *J. Nucl. Mater.* 480 (2016) 235–243.
- [25] C.M. Parish, in: P.W. Hawkes (Ed.), *Advances in Imaging and Electron Physics*, 168, 2011, pp. 249–295 Vol. 168.
- [26] R. van Bremen, D.R. Gomes, L. de Jeer, V. Ocelik, J.T.M. De Hosson, *Ultramicroscopy* 160 (2016) 256–264.
- [27] P.W. Trimby, Y. Cao, Z. Chen, S. Han, K.J. Hemker, J. Lian, X. Liao, P. Rottmann, S. Samudrala, J. Sun, *Acta Mater.* 62 (2014) 69–80.
- [28] G.C. Sneddon, P.W. Trimby, J.M. Cairney, *Mater. Sci. Eng. R. Rep.* 110 (2016) 1–12.
- [29] C.M. Parish, K. Wang, R.P. Doerner, M.J. Baldwin, *Scr. Mater.* 127 (2017) 132–135.
- [30] K. Wang, R.P. Doerner, M.J. Baldwin, F.W. Meyer, M.E. Bannister, A. Darbal, R. Stroud, *C.M. Parish, Sci. Rep.* 7 (2017) 42315.
- [31] L.N. Brewer, J.R. Michael, *Microscopy Today* 18 (2) (2010) 10–15.
- [32] K.G. Field, L.M. Barnard, C.M. Parish, J.T. Busby, D. Morgan, T.R. Allen, *J. Nucl. Mater.* 435 (1–3) (2013) 172–180.
- [33] E. Rauch, M. Véron, *Mater. Charact.* 98 (2014) 1–9.
- [34] X. Liu, D. Choi, H. Beladi, N.T. Nuhfer, G.S. Rohrer, K. Barmak, *Scr. Mater.* 69 (5) (2013) 413–416.
- [35] P.A. Midgley, A.S. Eggeman, *IUCrj* 2 (1) (2015) 126–136.

- [36] D. Viladot, M. Véron, M. Gemmi, F. Peiró, J. Portillo, S. Estradé, J. Mendoza, N. Llorca-Isern, S. Nicolopoulos, J. Microsc. 252 (1) (2013) 23–34.
- [37] M.K. Miller, K.F. Russell, D.T. Hoelzer, J. Nucl. Mater. 351 (1–3) (2006) 261–268.
- [38] B. Mazumder, X. Yu, P. Edmondson, C. Parish, M. Miller, H. Meyer, Z. Feng, J. Nucl. Mater. 469 (2016) 200–208.
- [39] Y. Miao, K. Mo, Z. Zhou, X. Liu, K.-C. Lan, G. Zhang, M.K. Miller, K.A. Powers, Z.-G. Mei, J.-S. Park, Mater. Sci. Eng. A 639 (2015) 585–596.
- [40] S. Piazolo, A. La Fontaine, P. Trimby, S. Harley, L. Yang, R. Armstrong, J.M. Cairney, Nat. Commun. 7 (2016).
- [41] A.J. Breen, K. Babinsky, A.C. Day, K. Eder, C.J. Oakman, P.W. Trimby, S. Primig, J.M. Cairney, S.P. Ringer, Microsc. Microanal. (2017) 1–12.
- [42] M. Herbig, P. Choi, D. Raabe, Ultramicroscopy 153 (2015) 32–39.
- [43] L.A. Giannuzzi, F.A. Stevie, Micron 30 (3) (1999) 197–204.
- [44] A. Aitkaliyeva, J.W. Madden, B.D. Miller, J.I. Cole, J. Gan, J. Nucl. Mater. 459 (2015) 241–246.
- [45] R. Cerchiara, P. Fischione, J. Liu, J. Matesa, A. Robins, H. Fraser, A. Genc, Microscopy Today 19 (01) (2011) 16–19.
- [46] P.D. Edmondson, A. London, A. Xu, D.E.J. Armstrong, S.G. Roberts, J. Nucl. Mater. 462 (2015) 369–373.
- [47] C.M. Parish, N.K. Kumar, L.L. Snead, P.D. Edmondson, K.G. Field, C. Silva, A.M. Williams, K. Linton, K.J. Leonard, Microsc. Microanal. 21 (S3) (2015) 1003–1004.
- [48] S.J. Zinkle, K.A. Terrani, J.C. Gehin, L.J. Ott, L.L. Snead, J. Nucl. Mater. 448 (2014) 374–379.
- [49] C.M. Parish, K.A. Terrani, Y.-J. Kim, T. Koyanagi, Y. Katoh, J. Eur. Ceram. Soc. 37 (4) (2017) 1261–1279.
- [50] P.D. Edmondson, M.K. Miller, K.A. Powers, R.K. Nanstad, J. Nucl. Mater. 489 (2017) 236–237.
- [51] P.D. Edmondson, M.K. Miller, K.A. Powers, R.K. Nanstad, J. Nucl. Mater. 470 (2016) 147–154.
- [52] C.M. Parish, T.J. Gerczak, P.D. Edmondson, K.A. Terrani, Microsc. Microanal. 22 (S3) (2016) 330–331.